molecules

MDPI

Review

Oxide Materials for Thermoelectric Conversion

Yucen Liu [1], Jun Zhi [1], Wannuo Li [1], Qian Yang [1,2,*], Long Zhang [1,*] and Yuqiao Zhang [1,*]

[1] Institute of Quantum and Sustainable Technology (IQST), School of Chemistry and Chemical Engineering, Jiangsu University, Zhenjiang 212013, China; yc_liu1999@163.com (Y.L.); 2222212112@stmail.ujs.edu.cn (J.Z.); lwn000119@163.com (W.L.)

[2] Foshan (Southern China) Institute for New Materials, Foshan 528200, China

* Correspondence: yangqian0730@foxmail.com (Q.Y.); longzhang@ujs.edu.cn (L.Z.); yuqiaozhang0730@hotmail.com (Y.Z.)

Abstract: Thermoelectric technology has emerged as a prominent area of research in the past few decades for harnessing waste heat and improving the efficiency of next-generation renewable energy technologies. There has been rapid progress in the development of high-performance thermoelectric materials, as measured by the dimensionless figure of merit ($ZT = S^2 \cdot \sigma \cdot \kappa^{-1}$). Several heavy-metal-based thermoelectric materials with commercial-level performance ($ZT = 1$) have so far been proposed. However, the extensive application of these materials still faces challenges due to their low thermal/chemical stability, high toxicity, and limited abundance in the Earth's crust. In contrast, oxide-based thermoelectric materials, such as ZnO, $SrTiO_3$, layered cobalt oxides, etc., have attracted growing interest as they can overcome the limitations of their heavy-metal-based counterparts. In this review, we summarize the recent research progress and introduce improvement strategies in oxide-based thermoelectric materials. This will provide an overview of their development history and design schemes, ultimately aiding in enhancing the overall performance of oxide-based thermoelectric materials.

Keywords: thermoelectrics; oxide; ZnO; $SrTiO_3$; layered cobalt oxides

check for updates

Citation: Liu, Y.; Zhi, J.; Li, W.; Yang, Q.; Zhang, L.; Zhang, Y. Oxide Materials for Thermoelectric Conversion. *Molecules* **2023**, *28*, 5894. https://doi.org/10.3390/molecules28155894

Academic Editor: Emmanuel Koudoumas

Received: 15 July 2023
Revised: 1 August 2023
Accepted: 4 August 2023
Published: 5 August 2023

Copyright: © 2023 by the authors. Licensee MDPI, Basel, Switzerland. This article is an open access article distributed under the terms and conditions of the Creative Commons Attribution (CC BY) license (https://creativecommons.org/licenses/by/4.0/).

1. Introduction

Following the progression of human civilization and industrialization, vast amounts of fossil fuels have been consumed for energy purposes [1]. However, due to the low efficiency of utilizing fossil fuels, only around 30% of the primary energy can be effectively harnessed, while more than 60% is wasted as heat [2]. Therefore, the exploration of new and efficient technologies for recycling waste heat is crucial to align with the sustainable world envisioned by the United Nations in 2015 [3].

Thermoelectrics has emerged as a promising technique for the reutilization of waste heat [4,5]. By leveraging the Seebeck effect, thermoelectric materials can directly convert a temperature gradient into electricity (Figure 1a) [6]. The performance of a thermoelectric material is commonly quantified by a dimensionless figure of merit known as ZT, which is defined as:

$$ZT = \frac{S^2 \sigma T}{\kappa}$$

where S, σ, κ, and T denote the Seebeck coefficient (or thermopower), electrical conductivity, thermal conductivity, and absolute temperature, respectively. The overall conversion efficiency (η) of a thermoelectric generator can be determined by ZT using the following relationship [1]:

$$\eta = \frac{\Delta T}{T_h} \cdot \frac{\sqrt{1+ZT} - 1}{\sqrt{1+ZT} + \frac{T_c}{T_h}}$$

where T_h, T_c, and ΔT are the temperature at the hot and cold sides, and the temperature gradient along the thermoelectric generator, respectively. In accordance with the second law

of thermodynamics, the maximum efficiency of the thermoelectric generators is constrained by the Carnot efficiency ($\Delta T/T_h$). As illustrated in Figure 1b, the conversion efficiency of the thermoelectric generators, with varying average ZT values (ZT_{avg}), is plotted against T_h while assuming a fixed T_c at room temperature (300 K). To maximize η, it is imperative to utilize thermoelectric materials with high ZT values. Typically, ZT~1 is considered the minimum threshold for the practical application of a thermoelectric material.

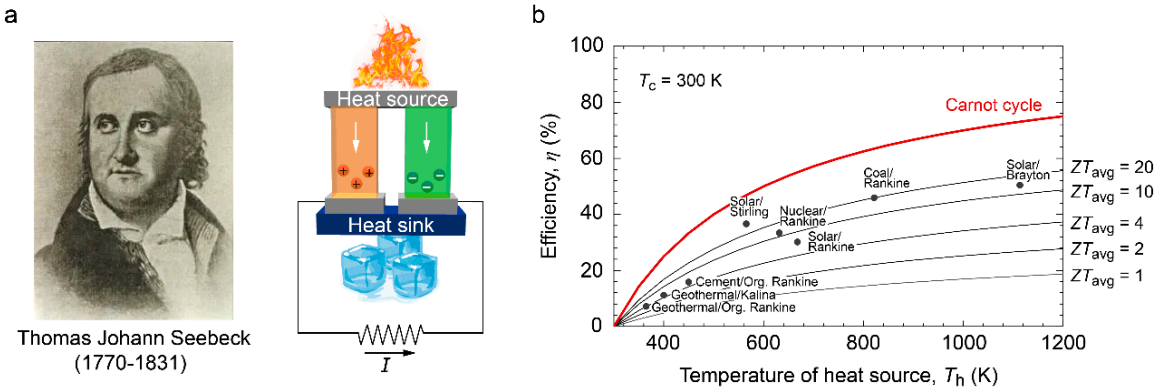


Figure 1. Schematic illustration of thermoelectric generators. (**a**) Thermoelectric power generation process based on the Seebeck effect, which was discovered by Thomas Johann Seebeck (1770–1831). Using a temperature gradient applied along the thermoelectric P-N junction, charge carriers inside the materials are driven from the hot side to the cold side, resulting in a current flow (I) through the circuit. (**b**) Power generation efficiency (η), as a function of the temperature of heat source (T_h), in the thermoelectric generators with different average ZT values (ZT_{avg}). The efficiency values for several heat engines currently being used are plotted for comparison. Reproduced with permission [7].

Thus far, a range of thermoelectric materials exhibiting high ZT values has been discovered, including filled skutterudites alloy [8], semi-Heusler intermetallic compounds [9], Bi_2Te_3 [10], Mg_3Sb_2 [11], GeTe [12], $AgPb_mSbTe_{2+m}$ [13], Cu_2Se [14], Cu_2S [15], SnSe [16–20], etc, primarily belonging to the chalcogenide family. However, despite advancements, the conversion efficiency of thermoelectric materials still falls short of meeting practical application requirements when compared to traditional energy conversion techniques [7]. Additionally, these materials face limitations in high-temperature usage (i.e., >700 °C) due to their low thermal and chemical stabilities. Furthermore, their low natural element abundance and high toxicity introduce uncertainties and challenges in their practical implementation.

To address these challenges, considerable attention has been directed toward oxide-based thermoelectrics as a potential solution. Oxide-based thermoelectric materials offer higher thermal and chemical robustness, making them more suitable for high-temperature applications. Moreover, as depicted in Figure 1b, the advantage of operating at high temperatures can offset some of the limitations associated with lower ZT values.

Extensive research on oxide-based thermoelectrics initially centered around investigating simple conducting oxides, such as CdO [21], NiO [22], ZnO [23], In_2O_3 [24], rutile-TiO_2 [25], SnO_2 [26], Cu_2O [27], and Fe_3O_4 [28]. This was followed by a subsequent surge of interest in cuprous oxide-based superconducting materials, such as La_2CuO_4 [29], La-Ba-Cu-O [30], $YBa_2Cu_3O_{7-\delta}$ [31], and Tl-Ca-Ba-Cu-O [32]. Recent studies have uncovered the potential of compounds, including $CaMnO_3$ [33], $Zn_{1-x}Al_xO$ [34], A_xCoO_2 (A_x = $Na_{0.75}$, $Ca_{0.33}$, $Sr_{0.33}$, $Ba_{0.33}$) [35–41], and $SrTiO_3$ [42–46]. This review provides an overview of the advancements in oxide-based thermoelectrics, with a particular focus on the development of several representative compounds and the recent effective methods employed by researchers to enhance their properties. Notably, the review delves into the progress made in ZnO, $SrTiO_3$, and layered cobaltates (A_xCoO_2, A_x = $Na_{0.75}$, $Ca_{0.33}$, $Sr_{0.33}$, $Ba_{0.33}$).

2. ZnO

ZnO is one of the most investigated oxides for photovoltaic, sensing, piezoelectric, and thermoelectric applications, with n-type semiconducting behaviors [34,47–50]. As shown in Figure 2a, ZnO crystals possess a wurtzite structure, where the Zn atom is surrounded by four oxygens, resulting in a hexagonal closely packed sublattice. In the solid state, ZnO acts as an insulator with a wide bandgap of about 3.2–3.5 eV. The conduction band minimum (CBM) is mainly derived from the 4s orbital in the Zn^{2+} ion, which shows a high carrier mobility. Pristine ZnO displays an increasing electrical conductivity with temperature due to the thermally excited electrons. Under ideal stoichiometric conditions, ZnO materials demonstrate a thermoelectric power factor ranging from 0.8 to 1 mW m^{-1} K^{-2}. However, due to the low electrical conductivity and high thermal conductivity (49 W m^{-1} K^{-1} at 300 K and 10 W m^{-1} K^{-1} at 1000 K [51]), the *ZT* value and overall efficiency of pristine ZnO are still limited in practical applications.

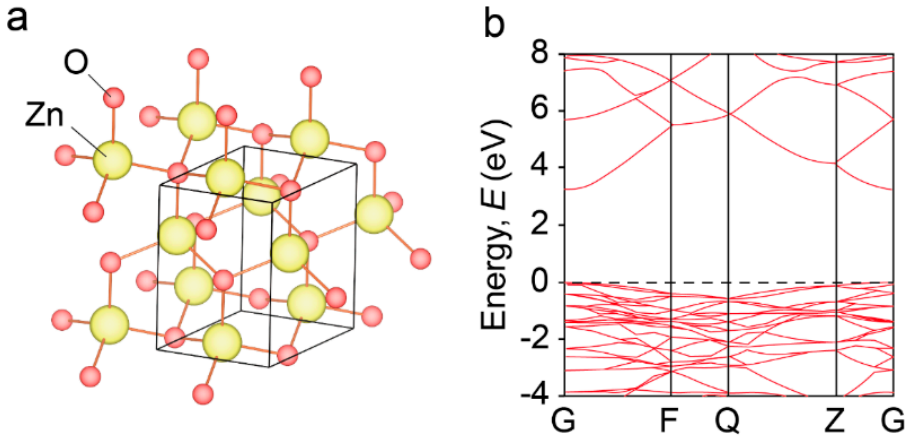


Figure 2. Schematic illustrations of (**a**) crystal structure and (**b**) electronic band structure of ZnO bulk materials. The pure ZnO exerts a wurtzite structure with a direct band gap of 3.3–3.5 eV [52].

In order to enhance the electrical characteristics of zinc oxide (ZnO), the introduction of donor dopants such as Al^{3+} and Ga^{3+} has been widely employed. A small number of dopants can tune the conduction behavior of ZnO from semiconducting to metallic. In 1996, Ohtaki and Tswbota reported on the high-temperature thermoelectric properties of Al-doped ZnO, exhibiting a thermoelectric figure of merit (*ZT*) of approximately 0.3 at 1273 K, along with a thermoelectric power factor ranging from 1 to 1.5 mW m^{-1} K^{-2}, which is comparable to traditional chalcogenide-based counterparts [34,50]. In 2011, Jood et al. prepared ZnO nanocomposites incorporating Al, further enhancing the *ZT* value to 0.44 at 1000 K [53]. In addition to Al, a diverse range of dopants, including Ga, Ni, Co, Fe, In, Ti, Mn, and Sb, have been utilized to improve either the overall or specific ZnO performance characteristics [54–56]. Furthermore, apart from their influence on electrical properties, elemental doping has proven effective in reducing the thermal conductivity in the ZnO system. As shown in Figure 3, Ohtaki et al. found that using a third element, Ga, co-doped with Al, could dramatically reduce the thermal conductivity, while having a relatively small effect on electrical conductivity [57]. With an obvious reduction in thermal conductivity and enhancement in power factor, the *ZT* value of the double-doped oxide in the composition of $Zn_{0.96}Al_{0.02}Ga_{0.02}O$ is 0.47 at 1000 K and 0.65 at 1247 K.

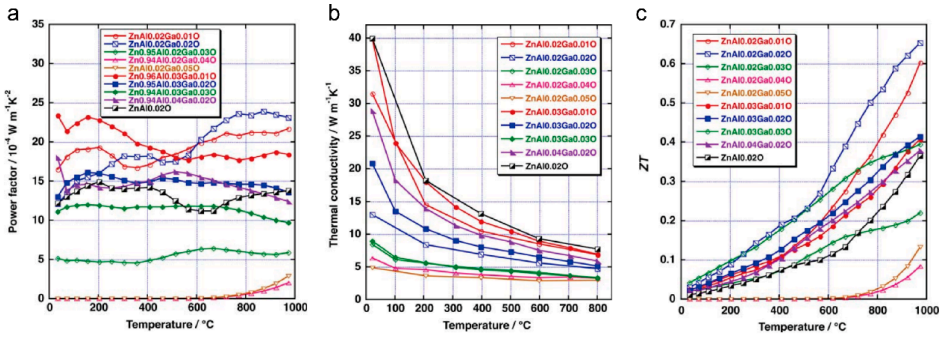


Figure 3. Thermoelectric properties of Al–Ga-co-doped ZnO. (**a**) Power factor. (**b**) Thermal conductivity. (**c**) *ZT* values. Reproduced with permission [57].

In 2021, utilizing the thermal conductivity reduction effect of the coating grain structure, Somnath Acharya et al. prepared ZnS-coated Al-doped compact ZnO nanostructures using the low-temperature co-precipitation method and spark plasma sintering (SPS), in which the Al doping increased the carrier concentration as well as optimizing the electron transport characteristics (Figure 4). The decrease in thermal conductivity can be attributed to the enhanced coherent phonon-scattering in $Zn_{1-x}Al_xO$. The power factor of the resulting 2% ZnS-coated $Zn_{0.98}Al_{0.02}O$ nanostructures exhibited a noteworthy enhancement of 161% compared to pure ZnO, reaching a value of 0.75 mW m^{-1} K^{-2}. Furthermore, a peak figure of merit (*ZT*) value of 0.2 was attained, which represents a remarkable 272% increase compared to pure ZnO [58].

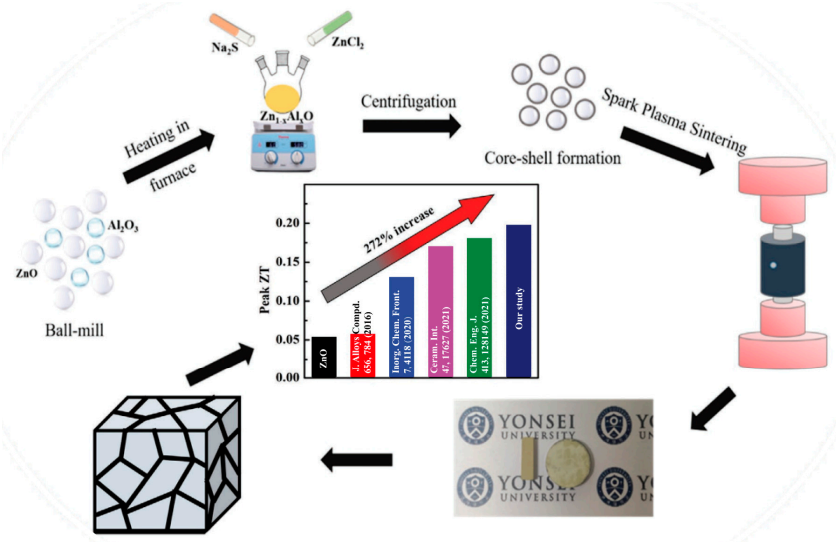


Figure 4. Schematic illustrating the synthesizing steps of ZnO-coated $Zn_{1-x}Al_xO$ samples demonstrating the high *ZT* values compared to previously reported Al-doped ZnO. Reproduced with permission [58].

More recently, as shown in Figure 5, Soumya Biswas et al. prepared ZnO nanocomposites using a simple solution-based method with both Al doping and reduced graphene oxide (RGO) encapsulation techniques. The influence of Al doping on the nanocomposites resulted in an increased electrical conductivity and decreased thermal conductivity, albeit accompanied by low Seebeck coefficient values. Furthermore, the incorporation of RGO inclusions into the nanocomposites yielded dual benefits. Firstly, it enhanced the overall electrical conductivity, contributing to improved charge transport properties. Secondly, through the phenomenon of energy filtration, the presence of RGO enhanced the Seebeck coefficient, promoting more favorable thermoelectric properties. Consequently, the synthe-

sized material exhibited a notable figure of merit (*ZT*) value of approximately 0.52 at an elevated temperature of 1100 K [59].

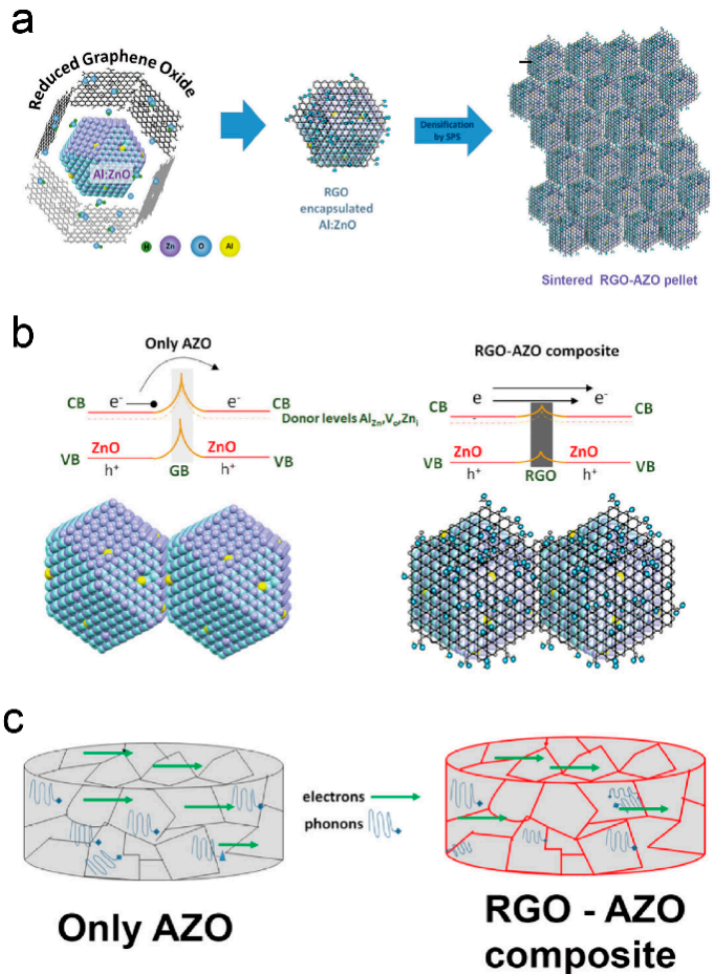


Figure 5. Schematic diagram of (**a**) formation of the RGO-encapsulated Al-doped ZnO composites (RGO–AZO). (**b**) Scattering and transport mechanisms in a densified ZnO–RGO composite across grain boundaries. (**c**) Scattering of phonons and electrons in bulk samples. Reproduced with permission [59].

In addition to the bulk state, recent progress has also been achieved in two-dimensional thin film-based ZnO materials. Zhou et al. prepared Ga-doped ZnO epitaxial thin films using pulsed laser deposition (PLD) technology. During the preparation process, growth rate, crystallinity, surface roughness, and even the Fermi level could be changed by controlling deposition temperature. The improved Ga doping efficiency resulted in an increased Hall mobility and higher carrier concentration, consequently, leading to a notable enhancement in electrical conductivity. Finally, GZO films deposited at 673 K showed the best quality and crystallinity, with a power factor of 256 mW m^{-1} K^{-2} [60]. In 2016, Shimizu et al. proposed that the thermoelectric performance of ZnO could be enhanced by a two-dimensional electron gas in the ion gel-gated field-effect transistor (Figure 6a) [61]. The accumulation of an ~1 nm 2D electron gas at the surface of ZnO can significantly enhance the Seebeck coefficient (Figure 6b), which brings about an obviously increased power factor compared to the bulk counterparts [62–65].

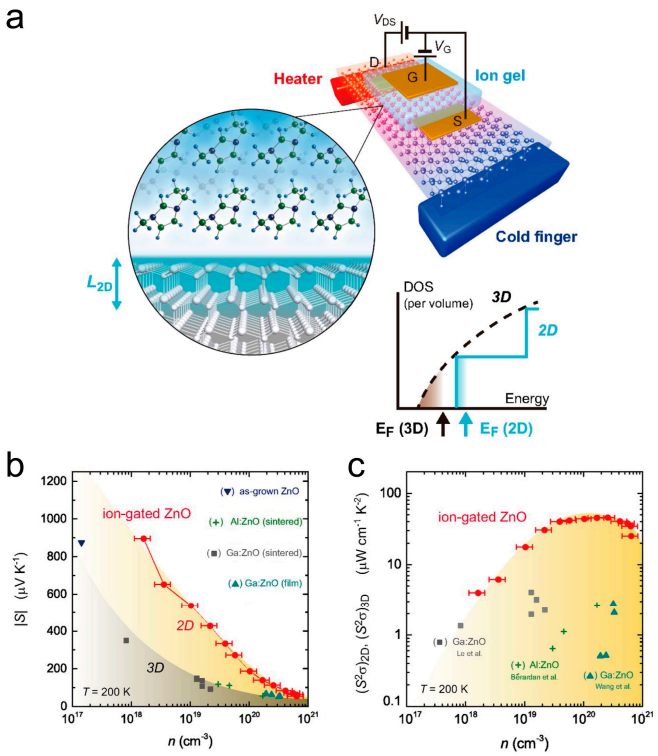


Figure 6. Two-dimensional electron gas accumulated at the surface of ZnO boosts the thermoelectric performance. (**a**) Schematic structure of ZnO-based ion-gated transistor. (**b**) Carrier concentration (n) dependence on Seebeck coefficient (S) at 200 K. The values of $|S|$ in the ion-gated ZnO were larger than in bulk ZnO [62–65]. (**c**) Carrier concentration dependence of thermoelectric power factor ($S^2\sigma$). The ion-gated ZnO showed larger values than the bulk ZnO, as expected from the enhanced S. Reproduced with permission [61].

3. $SrTiO_3$

$SrTiO_3$ is considered a promising n-type oxide thermoelectric material with a high Seebeck coefficient due to the large effective mass of the Ti 3D orbital [43]. Meanwhile, its high melting point also makes it a thermoelectric candidate at high temperatures. As shown in Figure 7, $SrTiO_3$ has a simple cubic-perovskite crystal structure (lattice parameter, a = 3.905 Å). $SrTiO_3$ behaves as an insulator, characterized by a very low carrier concentration, poor electron transport, and high thermal conductivity. Therefore, to enhance the thermoelectric performance of $SrTiO_3$, two crucial aspects necessitate attention: optimizing the carrier concentration and reducing thermal conductivity. $SrTiO_3$ possesses a high relative dielectric constant (ε_r~220 at room temperature), and the impurity orbitals start to overlap at a rather low donor doping level (~0.5 mol%), resulting in a metallic electron transport property in $SrTiO_3$ [43]. In this case, it is easy to introduce dopants (i.e., La^{3+} and Nb^{5+}) into the $SrTiO_3$ matrix and modulate the thermoelectric properties.

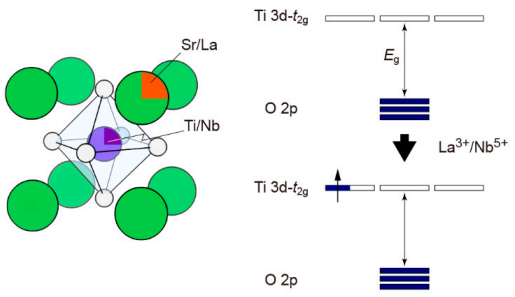


Figure 7. Schematic illustration of the $SrTiO_3$ lattice structure and doping mechanism.

In addition to the common donor dopant La^{3+} and Nb^{5+}, other elements are also utilized to tailor the carrier concentration, lattice constant, defect level, and lattice distortion. In the A-site doping, common elements included La, Y, Na, Ce, Mn, Bi, Nd, Pr, Sm, Gd, Dy, etc. [5,66]. At the B-site, common doping elements included Nb, Ta, Se, V, Cr, Fe, Co, Ni, In, Sb, Mg, etc. Ru, Al, etc. [67]. In 2001, Okuda first found that the power factor of $Sr_{1-x}La_xTiO_3$ was 28–36 mW $cm^{-1}k^{-2}$, which is comparable to traditional alloy-type thermoelectric material Bi_2Te_3 at room temperature, although its ZT was still <1 due to its excessive thermal conductivity (Figure 8). Despite this limitation, the notable power factor exhibited by $Sr_{1-x}La_xTiO_3$ proved its potential for application in thermoelectric systems [42].

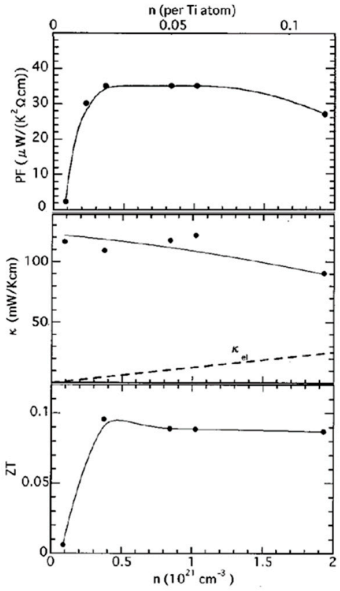


Figure 8. Carrier concentration (n) dependence of power factor (PF) thermal conductivity (κ), and ZT value at room temperature in $Sr_{1-x}La_xTiO_3$. Solid lines are guides to the eye and the dashed line represents the electronic thermal conductivity (κ_{el}), estimated by the Wiedemann–Franz law. Reproduced with permission [42].

Co-doping on both the Sr site and Ti site is a widely employed strategy in the field. In 2017, Wang et al. successfully overcame the challenges associated with nanoscale co-doping of Nb and La by integrating the hydrothermal method with efficient sintering techniques. Using this approach, they achieved precise control over the co-doping process, resulting in the precipitation of nano-inclusions during the sintering phase and the formation of a complex microstructure. Consequently, the Seebeck coefficient was significantly enhanced, while the thermal conductivity was effectively reduced. Finally, a record-high ZT of >0.6 was generated at 1000–1100 K in the 10 mol% La and 10 mol% Nb-doped $SrTiO_3$ bulk materials [46]. More recently, Acharya et al. proposed thermoelectric composites of Nb-doped $SrTiO_3$ using natural graphite, which possessed surged electrical conductivity, while restraining thermal conductivity (Figure 9). The ZT value can reach 1.42 at ~1050 K and keep within >1.2 of a broad temperature range (850–1050 K) [68].

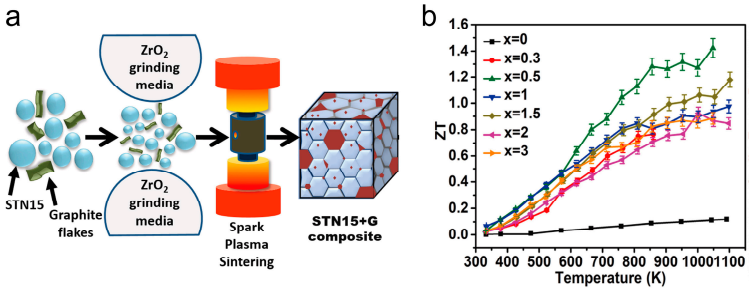


Figure 9. Schematic representation of processing bulk $SrTi_{0.85}Nb_{0.15}O_3$ matrix (STN) oxide composites with graphite inclusions (**a**) and temperature-dependent *ZT* values for sintered STN + *x* wt% graphite composites ($0 \leq x \leq 3$) (**b**). Reproduced with permission [68].

In addition to common doping, low-dimensional is another effective strategy to improve thermoelectric performance. In thin film cases, phonon scatterings at the interface and surface areas will be much more obvious than in the bulk state. In 2021, Zhang et al. prepared La- and Nb-doped $SrTiO_3$ full-range solid solution epitaxial films by the PLD method and investigated their thermoelectric phase diagrams at room temperature (Figure 10) [69,70]. Both $SrTiO_3$–$LaTiO_3$ and $SrTiO_3$–$SrNbO_3$ solid solutions displayed a similar power factor ($=S^2 \cdot \sigma$) changing pattern, which peaked at the carrier concentration (n) of around 10^{21} cm^{-3}, while different thermal conductivity variation tendencies, especially at the substitution level, were above 50 mol%. The authors attributed this to the different lattice distortions in the two solid solution systems. Modulation of the thermal conductivity through doping achieved a much larger *ZT* value of ~0.11 at room temperature compared to previous reports [71].

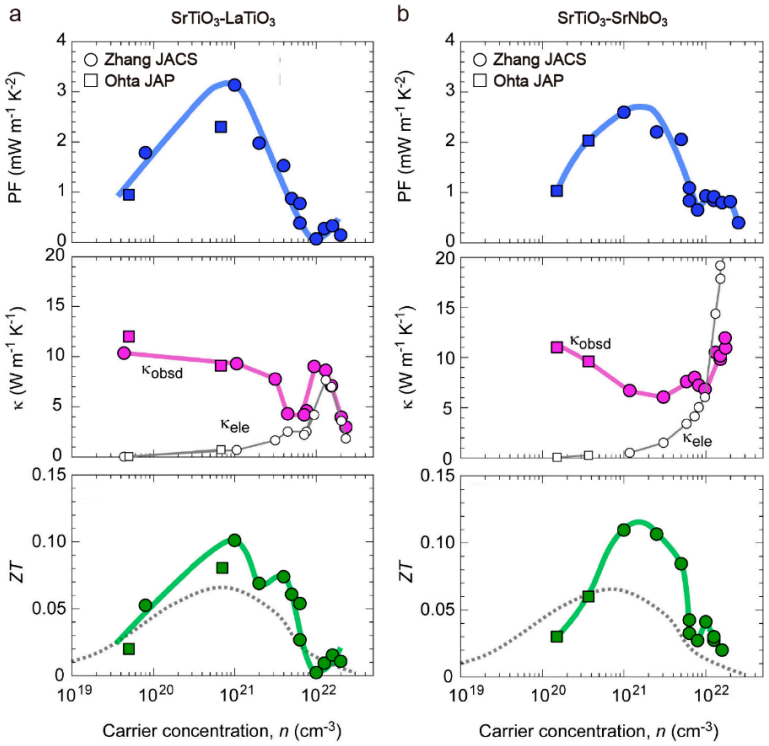


Figure 10. Power factor (PF), thermal conductivity (κ), and *ZT* values for $SrTiO_3$–$LaTiO_3$. (**a**) and $SrTiO_3$–$SrNbO_3$ (**b**) solid solutions. La^{3+} and Nb^{3+} substitutions result in a similar power factor behavior and a rather different tendency in thermal conductivity due to the different lattice distortions. The *ZT* value of $SrTiO_3$-based epitaxial films reached 0.11 at room temperature. The solid line is a guide for eyes. The dotted lines are the values of bulk single crystals. Reproduced with permission [43,71].

In 1993, Dresselhaus et al. published their findings that the two-dimensional electron system (2DES) can enhance thermopower without sacrificing electrical conductivity, which significantly boosted the *ZT* value [72]. As shown in Figure 11a, the absolute value of thermopower is proportional to the energy differential in the density of the state:

$$|S| \propto \left[\frac{\partial DOS(E)}{\partial E}\right]_{E=E_F}$$

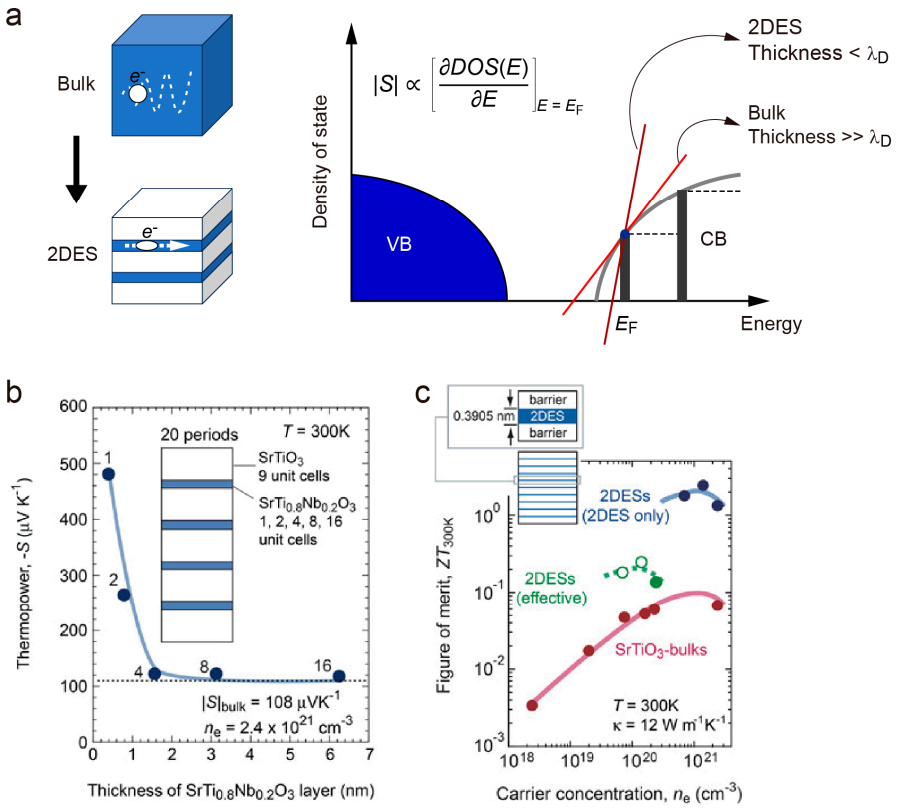


Figure 11. Enhancing thermopower through the two-dimensional electron system (2DES). (**a**) Schematic illustration of the 2DES enhanced thermopower mechanism while holding a good transport property. (**b**) Room temperature thermopower versus quantum well thickness in the $SrTi_{0.8}Nb_{0.2}O_3$ | $SrTiO_3$ superlattice. An obvious boost in thermopower can be observed when the thickness of the $SrTi_{0.8}Nb_{0.2}O_3$ quantum well is smaller than 1.56 nm (four-unit cells of $SrTiO_3$). (**c**) Carrier concentration-dependent *ZT* values at room temperature. The *ZT* value of the $SrTi_{0.8}Nb_{0.2}O_3$ quantum well reaches ~2.4. Reproduced with permission [73].

As the thickness of the 2DES decreases below the de Broglie Wavelength, the conduction band (CB) will split, which results in an enhancement of thermopower. In 2007, Ohta et al. fabricated the $SrTi_{0.8}Nb_{0.2}O_3$ | $SrTiO_3$ superlattice structure and confirmed the 2DES enhancement effect in thermopower by decreasing the thickness of the quantum wells (Figure 11b) [73]. A *ZT* value of ~2.4 was achieved in the 2DES (Figure 11c).

In order to achieve a stronger enhancement effect, Dresselhaus et al. proposed the concept of using materials with longer de Broglie wavelengths in quantum well constructions [74]. Based on this concept, Zhang et al. utilized the tunable de Broglie wavelength in the $SrTiO_3$–$SrNbO_3$ full-range solid solution when constructing superlattices [69]. With a longer de Broglie wavelength, the superlattice structures achieved superior overall thermoelectric performances over the bulk counterparts [75]. As shown in Figure 12a, the 2DES exerts a much higher enhancement factor (S_{2DES}/S_{Bulk}) in the thermopower, where the 2DES with a longer de Broglie wavelength reached 10, which is ~2 times larger than the 2DESs, which has a shorter de Broglie wavelength. Meanwhile, a longer de Broglie

wavelength better maintains the better electron-transport property. As a result, the highest power factor in the superlattices reached ~5 mW m^{-1} K^{-2}, thereby reaching 200% of the bulk counterparts (Figure 12b).

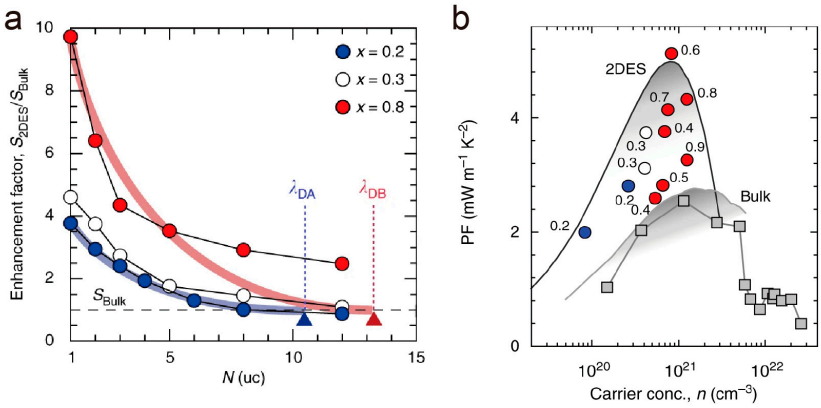


Figure 12. Longer de Broglie wavelength creates a larger enhancement in thermoelectric performance. (**a**) Enhancement factors in thermopower (S_{2DES}/S_{Bulk}) for three sets of [N uc $SrTi_{1-x}Nb_xO_3$ | 11 uc $SrTiO_3$]$_{10}$ 2DESs. For x = 0.2 and 0.3 2DESs, the highest S_{2DES}/S_{Bulk} values are obtained at N = 1, which are 4 and 5, respectively, while that of x = 0.8 can reach 10. (**b**) Double enhancement of power factor (PF) is seen when x = 0.6 (5.1 mW m^{-1} K^{-2} at n~8 × 10^{20} cm^{-3}). Reproduced with permission [75].

More recently, the strategy of high-entropy alloying has been applied to increase the thermoelectric performance of $SrTiO_3$-based materials, where multiple metal ions are introduced to the A-site or B-site of the $SrTiO_3$ lattice to induce more anharmonicity and multiphonon scattering, while the lattice thermal conductivity can be significantly suppressed. Banerjee et al. mixed five transition metal elements at the B-site in the $SrTiO_3$, synthesizing $Sr(Ti_{0.2}Fe_{0.2}Mo_{0.2}Nb_{0.2}Cr_{0.2})O_3$ high-entropy perovskite ceramics. The thermal conductivity can be reduced to 0.7 W m^{-1} K^{-1} at 1100 K [76]. Zheng et al. fabricated the A-site high-entropy $SrTiO_3$-based thermoelectric ceramics [77]. Ca, Sr, Ba, Pb, and La were introduced to induce a large lattice distortion and a huge mass fluctuation effect, which resulted in a minimum thermal conductivity of 1.17 W m^{-1} K^{-1} at 923 K. Using newer concepts combined with traditional oxide-based materials, a chance remains to further increase their thermoelectric performance.

4. Layered Cobalt Oxides (A_xCoO_2 (A_x = $Na_{0.75}$, $Ca_{0.33}$, $Sr_{0.33}$, $Ba_{0.33}$))

Layered cobalt oxides (A_xCoO_2) exert a sandwich structure composed of CoO_2 and A-site cations by stacking layer by layer (Figure 13). The conduction path is dependent on the CoO_2 layer, which displays a large Seebeck coefficient due to the low-spin state of Co^{3+} [78]. It has been theoretically and experimentally proven that the spin entropy flow generated from the electronic conduction between Co^{3+} and Co^{4+} majorly contributes to the enhancement of the thermoelectric potential of A_xCoO_2-based oxide materials [78–81]. At high temperatures, the Seebeck coefficient (S) can be calculated based on the Koshibae equation:

$$S\ (T \to \infty) = -\frac{k_B}{e} \ln \left[\frac{g\left(Co^{4+}\right)}{g\left(Co^{3+}\right)} \frac{n_{Co^{4+}}}{n_{Co^{3+}}} \right]$$

where k_B is the Boltzmann constant, e is the electronic unit charge, g is the different possible ways in which electrons can be arranged in the orbitals of Co^{3+} and Co^{4+} ions, and n is the concentration of a given Co species. Additionally, g is the product of the spin degeneracy (g_s) and orbital (g_o) degeneracy: $g = g_s \ldots g_o$, whereby $g_s = 2\zeta + 1$, where ζ is the ions' total spin number and g_o is the number of valid permutations for distributing the electrons across

its orbitals. Using electronic conduction through hopping in Na_xCoO_2, a spin entropy flow occurs in the opposite direction [82]. Therefore, the contribution of the spin entropy to the thermoelectric potential in the cobalt oxide group is related to the concentration of the Co^{4+} and Co^{3+} ions, as well as the degree of the spin degeneracy of Co ions. Since a decrease in the Co^{4+} concentration will lead to an increase in spin entropy; thus, the manipulation of the Co^{4+} ion concentration through excessive metal doping has emerged as an effective approach to modulating the spin entropy contribution. Using the ion exchange process, the A-site cations can be tuned from Na^{2+} to Ca^{2+}, Sr^{2+}, and Ba^{2+} and accompanied by a topotactic phase transition.

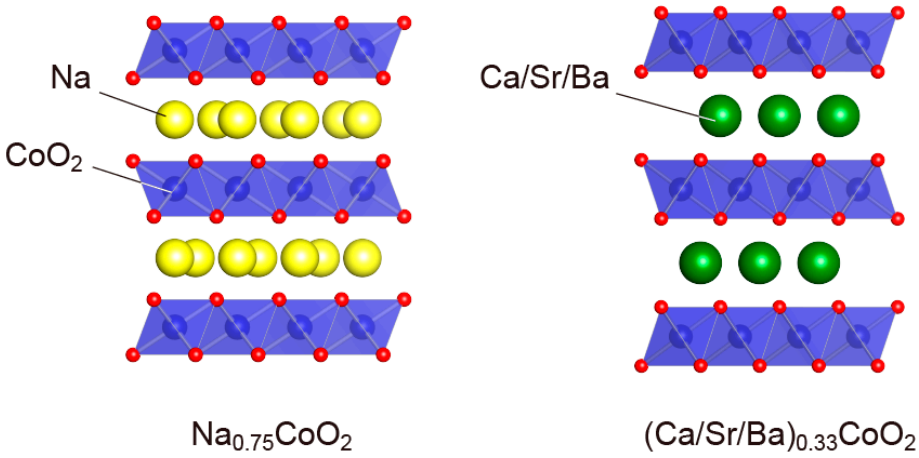


Figure 13. Schematic illustration of the layered cobaltite crystal structure (A_xCoO_2 (A_x = $Na_{0.75}$, $Ca_{0.33}$, $Sr_{0.33}$, $Ba_{0.33}$)).

In 1997, Terasaki et al. discovered that $Na_{0.5}CoO_2$ crystal was a good candidate for thermoelectric application [35]. Compared to the traditional alloy-type materials Bi_2Te_3, it was found that their power factors are in the same order of magnitude. Meanwhile, the conductivity of Na_xCoO_2 is nearly four times that of Bi_2Te_3 [35,83]. In terms of thermal conductivity, the interface between layers affects heat transfer and contributes to the reduction in lattice thermal conductivity. Therefore, the large Seebeck coefficient and high electrical conductivity also indicate that the layered $Na_{0.5}CoO_2$ crystal is a kind of oxide-based thermoelectric material with research significance and prospect. The discovery has also drawn the attention of researchers to various metallic layered cobalt oxide-based thermoelectric materials.

However, constrained by the high thermal conductivity, the overall thermoelectric performance, *ZT* value, of $Na_{0.5}CoO_2$ is still far from the commercial level. In 2020, Cho et al. proposed that thermal conductivity can be suppressed significantly by substituting A-site ions in A_xCoO_2 from light ions to heavy ions [84]. Using heavier A-site ions will create a mismatch in phonon vibration modes between CoO_2 and the A-site cation layers, which will reduce the phonon mean free path and phonon group velocity, and therefore, the thermal conductivity (Figure 14a). They fabricated A_xCoO_2 (A_x = Li_1, $Na_{0.75}$, $Ca_{0.33}$, $Sr_{0.33}$, $La_{0.3}$) epitaxial films using the PLD method followed by the reactive solid phase epitaxy (R-SPE) method and ion exchange process. The thermal conductivity tendency was good after following the hypothesis along the in-plane direction, suggesting that the thermoelectric performance of A_xCoO_2-based materials can be enhanced through an elaborate modification of the A-site ions.

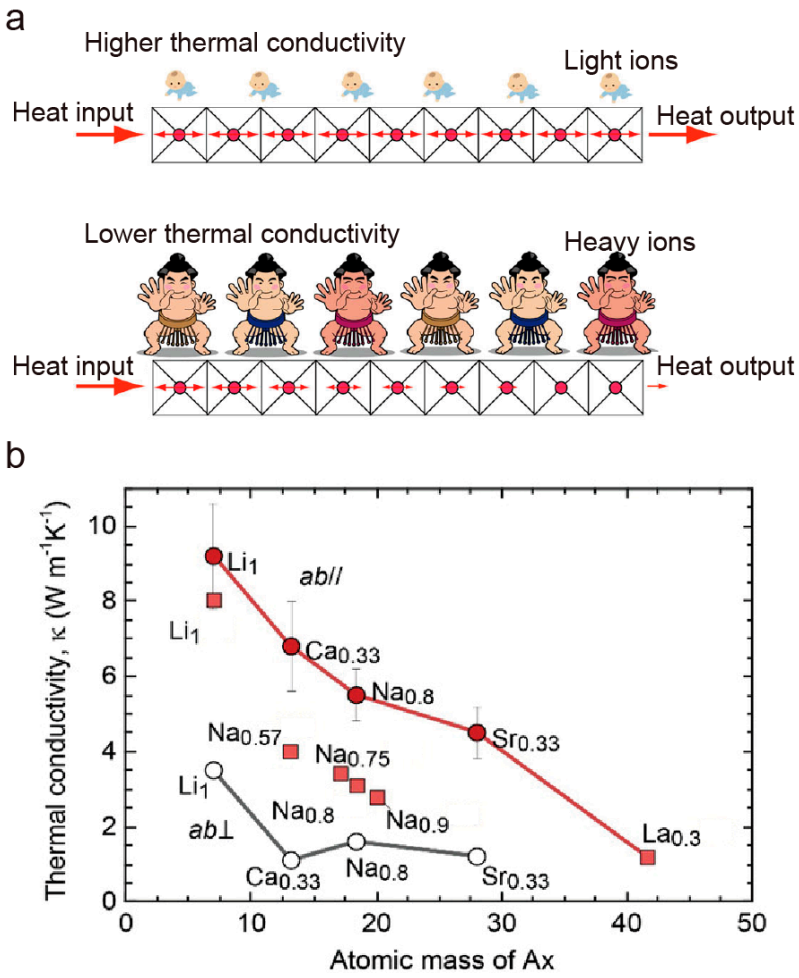


Figure 14. Reduction in thermal conductivity through heavy ion substitution at the A_xCoO_2 A-site. (**a**) Schematic phonon propagation of A_xCoO_2. Heavy ions (sumo wrestler) display a stronger thermal conductivity suppression effect than light ions (baby). (**b**) Anisotropic thermal conductivities of A_xCoO_2. As the mass of A-site ions increases, the in-plane thermal conductivity ($\kappa_{||}$) and cross-plane thermal conductivity ($\kappa_{\perp}$) decrease in tendency. Reproduced with permission [84].

Following this strategy, Takashima et al. checked the thermoelectric properties of A_xCoO_2 (A_x = $Na_{0.75}$, $Ca_{0.33}$, $Sr_{0.33}$, $Ba_{0.33}$) epitaxial films along the in-plane direction [40]. As shown in Figure 15, the power factor stays almost unchanged as the A-site ion mass increases, while the thermal conductivity is effectively suppressed, which suggests that the A-site ion exchange will not affect the electrical conduction path along the CoO_2 layer and only reduce their thermal transport properties. It also needs to be emphasized that A_xCoO_2 shows an A-site ion arrangement evolution with temperature. For example, $Ca_{0.33}CoO_2$ exerts a phase transition from a $\sqrt{3}a \times \sqrt{3}a$ hexagonal superstructure to a $2a \times \sqrt{3}a$ orthorhombic superstructure as the temperature increases above 400 °C [85]. However, in the $Ba_{0.33}CoO_2$ lattice, a mixture of orthorhombic and hexagonal superstructures can be maintained within a wide temperature range. This lattice disorder contributes significantly to phonon scattering and thermal conductivity reduction. A peak ZT value of ~ 0.11 was realized in the $Ba_{0.33}CoO_2$ epitaxial film at room temperature, which is a record high among the reported "reliable" ZT values in conducting oxides.

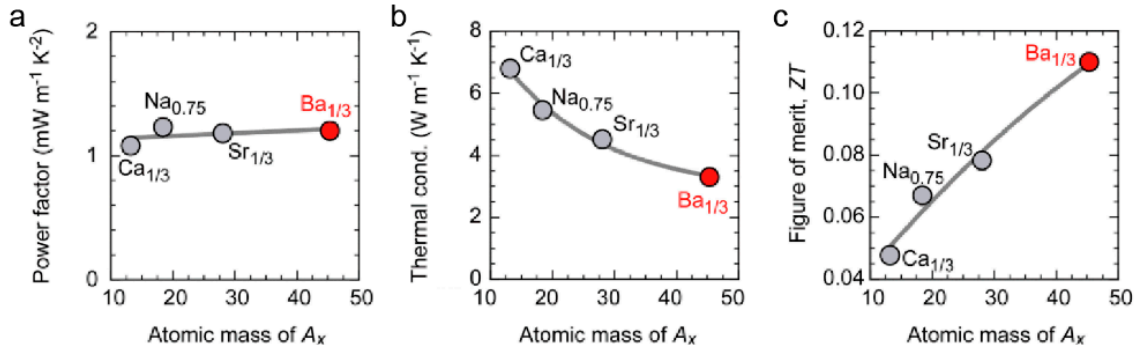


Figure 15. Thermoelectric properties of A_xCoO_2 epitaxial films at room temperature. (**a**) Power factor, (**b**) thermal conductivity, and (**c**) *ZT* values. The thermal conductivity decreases with A-site ion mass, while the power factor stays constant. The *ZT* value of $Ba_{0.33}CoO_2$ epitaxial film is ~0.11. Reproduced with permission [40].

As indicated in the report by Takashima et al., $Ba_{0.33}CoO_2$ is a promising thermoelectric material with superior performance to other counterparts. Later, Zhang et al. tested the high-temperature thermoelectric properties of A_xCoO_2 (A_x = $Na_{0.75}$, $Ca_{0.33}$, $Sr_{0.33}$, $Ba_{0.33}$) epitaxial films to confirm the application of $Ba_{0.33}CoO_2$ at elevated temperature environments [41]. They found a relatively high thermal stability of $Ba_{0.33}CoO_2$ up to 650 °C in air compared to other counterparts, by checking the room temperature resistivity after heat treatment in air at elevated temperatures (Figure 16a). High thermal stability makes it possible to measure thermoelectric properties of $Ba_{0.33}CoO_2$ up to 600 °C, with a *ZT* value of 0.55 at 600 °C (Figure 16b), comparable to those of PbTe and p-type SiGe (Figure 16c), which indicates $Ba_{1/3}CoO_2$ as a good candidate for high-temperature thermoelectric applications.

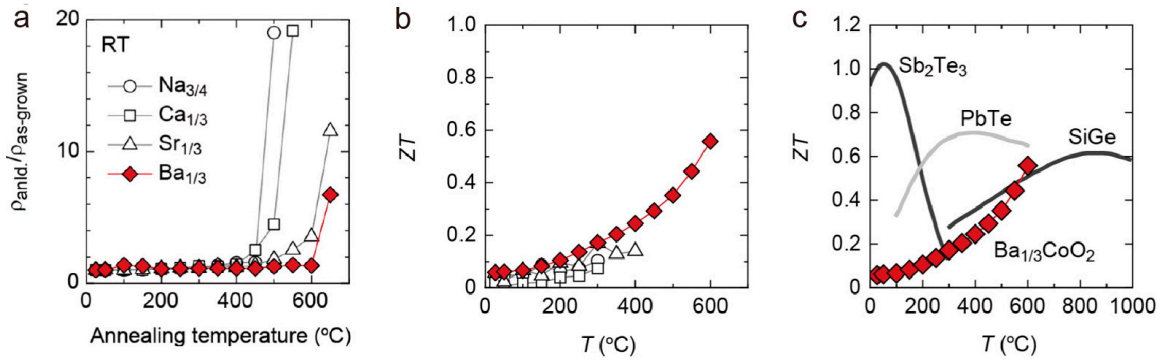


Figure 16. Thermal stability and thermoelectric properties of A_xCoO_2 (A_x = $Na_{3/4}$, $Ca_{1/3}$, $Sr_{1/3}$, and $Ba_{1/3}$) epitaxial films. (**a**) Resistivity was measured at room temperature after annealing at high temperatures for 0.5 h in air. (**b**) Temperature-dependent ZT values compared among the four A_xCoO_2 (A = $Na_{3/4}$, $Ca_{1/3}$, $Sr_{1/3}$, and $Ba_{1/3}$) films and (**c**) against commercially available p-type thermoelectric materials. Reproduced with permission [41].

5. Summary and Perspective

The recent advancements in oxide-based thermoelectric materials, with a focus on ZnO, $SrTiO_3$, and layered cobalt oxides, are reviewed, as they have garnered increasing attention due to their advantages over the chalcogenide family. The combination of high thermal/chemical stabilities and abundant elements on Earth makes thermoelectric oxides a highly promising candidate for numerous applications in waste heat recycling at elevated temperatures. Until now, these materials have witnessed revolutionary breakthroughs in performance enhancement through conventional doping and nanostructuring techniques. Additionally, the concept of low-dimensionalization has emerged as a new approach to further improve efficiency, especially in the context of device miniaturization and flexibility.

With the implementation of novel strategies aimed at enhancing the performance of thermoelectric oxides, such as augmenting the power factor through low-dimensionalization and reducing thermal conductivity via high-entropy alloying, oxide-based thermoelectric materials are poised to undergo significant advancements in the foreseeable future.

Funding: Y.Z. is supported by the National Natural Science Foundation of China (Grant No. 52202242), the Ministry of Science and Technology of PRC (Grant No. G2022014136L), the National Science Foundation of the Jiangsu Higher Education Institutions of China (Grant No. 22KJB430002), and the Start-Up Fund of Jiangsu University (Grant No. 5501310015). Q.Y. is supported by the support from Guangdong Basic and Applied Basic Research Foundation (Grant No. 2022A1515111067) and the Start-Up Fund of Jiangsu University (Grant No. 5501310025). L.Z. is supported by the Natural Science Foundation for Young Scholars of Jiangsu Province (Grant No. BK20210744) and the Start-Up Fund of Jiangsu University (Grant No. 4111310027).

Conflicts of Interest: The authors declare no conflict of interest. All authors have read and agreed to the published version of the manuscript.

References

1. Snyder, G.J.; Toberer, E.S. Complex thermoelectric materials. *Nat. Mater.* **2008**, *7*, 105–114. [CrossRef]
2. Wang, L.; Zhang, Z.; Liu, Y.; Wang, B.; Fang, L.; Qiu, J.; Zhang, K.; Wang, S. Exceptional thermoelectric properties of flexible organic−inorganic hybrids with monodispersed and periodic nanophase. *Nat. Commun.* **2018**, *9*, 3817. [CrossRef]
3. Griggs, D.; Stafford-Smith, M.; Gaffney, O.; Rockström, J.; Öhman, M.C.; Shyamsundar, P.; Steffen, W.; Glaser, G.; Kanie, N.; Noble, I. Sustainable development goals for people and planet. *Nature* **2013**, *495*, 305–307. [CrossRef]
4. Rowe, D.M. *CRC Handbook of Thermoelectrics*; CRC Press: Boca Raton, FL, USA, 1995.
5. Goldsmid, H.J. *Introduction to Thermoelectricity*; Springer: Berlin/Heidelberg, Germany, 2010.
6. Seebeck, T. Abh. K. *Akad. Wiss* **1823**, *265*, 1822.
7. Vining, C.B. An inconvenient truth about thermoelectrics. *Nat. Mater.* **2009**, *8*, 83–85. [CrossRef] [PubMed]
8. Rull-Bravo, M.; Moure, A.; Fernández, J.F.; Martín-González, M. Skutterudites as thermoelectric materials: Revisited. *RSC Adv.* **2015**, *5*, 41653–41667. [CrossRef]
9. Quinn, R.J.; Bos, J.-W.G. Advances in half-Heusler alloys for thermoelectric power generation. *Mater. Adv.* **2021**, *2*, 6246–6266. [CrossRef]
10. Scheele, M.; Oeschler, N.; Veremchuk, I.; Peters, S.-O.; Littig, A.; Kornowski, A.; Klinke, C.; Weller, H. Thermoelectric Properties of Lead Chalcogenide Core-Shell Nanostructures. *Acs Nano* **2011**, *5*, 8541–8551. [CrossRef]
11. Zhang, J.; Song, L.; Pedersen, S.H.; Yin, H.; Hung, L.T.; Iversen, B.B. Discovery of high-performance low-cost n-type Mg_3Sb_2-based thermoelectric materials with multi-valley conduction bands. *Nat. Commun.* **2017**, *8*, 13901. [CrossRef]
12. Liu, W.D.; Wang, D.Z.; Liu, Q.; Zhou, W.; Shao, Z.; Chen, Z.G. High-Performance GeTe-Based Thermoelectrics: From Materials to Devices. *Adv. Energy Mater.* **2020**, *10*, 2000367. [CrossRef]
13. Hsu, K.F.; Loo, S.; Guo, F.; Chen, W.; Dyck, J.S.; Uher, C.; Hogan, T.; Polychroniadis, E.K.; Kanatzidis, M.G. Cubic $AgPb_mSbTe_{2+m}$: Bulk Thermoelectric Materials with High Figure of Merit. *Science* **2004**, *303*, 818–821. [CrossRef]
14. Liu, H.; Shi, X.; Xu, F.; Zhang, L.; Zhang, W.; Chen, L.; Li, Q.; Uher, C.; Day, T.; Snyder, G.J. Copper ion liquid-like thermoelectrics. *Nat. Mater.* **2012**, *11*, 422–425. [CrossRef] [PubMed]
15. He, Y.; Day, T.; Zhang, T.; Liu, H.; Shi, X.; Chen, L.; Snyder, G.J. High Thermoelectric Performance in Non-Toxic Earth-Abundant Copper Sulfide. *Adv. Mater.* **2014**, *26*, 3974–3978. [CrossRef] [PubMed]
16. Zhao, L.-D.; Lo, S.-H.; Zhang, Y.; Sun, H.; Tan, G.; Uher, C.; Wolverton, C.; Dravid, V.P.; Kanatzidis, M.G. Ultralow thermal conductivity and high thermoelectric figure of merit in SnSe crystals. *Nature* **2014**, *508*, 373–377. [CrossRef]
17. Zhao, L.-D.; Tan, G.; Hao, S.; He, J.; Pei, Y.; Chi, H.; Wang, H.; Gong, S.; Xu, H.; Dravid, V.P.; et al. Ultrahigh power factor and thermoelectric performance in hole-doped single-crystal SnSe. *Science* **2016**, *351*, 141–144. [CrossRef]
18. Chang, C.; Wu, M.; He, D.; Pei, Y.; Wu, C.-F.; Wu, X.; Yu, H.; Zhu, F.; Wang, K.; Chen, Y.; et al. 3D charge and 2D phonon transports leading to high out-of-plane *ZT* in n-type SnSe crystals. *Science* **2018**, *360*, 778–783. [CrossRef]
19. Zhou, C.; Lee, Y.K.; Yu, Y.; Byun, S.; Luo, Z.-Z.; Lee, H.; Ge, B.; Lee, Y.-L.; Chen, X.; Lee, J.Y.; et al. Polycrystalline SnSe with a thermoelectric figure of merit greater than the single crystal. *Nat. Mater.* **2021**, *20*, 1378–1384. [CrossRef]
20. Su, L.; Wang, D.; Wang, S.; Qin, B.; Wang, Y.; Qin, Y.; Jin, Y.; Chang, C.; Zhao, L.-D. High thermoelectric performance realized through manipulating layered phonon-electron decoupling. *Science* **2022**, *375*, 1385–1389. [CrossRef]
21. Hogarth, C.A.; Andrews, J.P. XXV. Variation with oxygen pressure of the thermoelectric power of cadmium oxide. *Lond. Edinb. Dublin Philos. Mag. J. Sci.* **1949**, *40*, 273–282. [CrossRef]
22. Parravano, G. Thermoelectric behavior of nickel oxide. *J. Chem. Phys.* **1955**, *23*, 5–10. [CrossRef]
23. Hutson, A. Electronic properties of ZnO. *J. Phys. Chem. Solids* **1959**, *8*, 467–472. [CrossRef]
24. Arvin, M. Electrical conductivity and thermoelectric power of indium oxide. *Phys. Chem. Solids* **1962**, *23*, 1681–1683. [CrossRef]
25. Thurber, W.; Mante, A. Thermal Conductivity and Thermoelectric Power of Rutile (TiO_2). *Phys. Rev.* **1965**, *139*, A1655. [CrossRef]

26. Marley, J.; Dockerty, R. Electrical properties of stannic oxide single crystals. *Phys. Rev.* **1965**, *140*, A304. [CrossRef]
27. Young, A.; Schwartz, C. Electrical conductivity and thermoelectric power of Cu_2O. *J. Phys. Chem. Solids* **1969**, *30*, 249–252. [CrossRef]
28. Griffiths, B.; Elwell, D.; Parker, R. The thermoelectric power of the system $NiFe_2O_4$-Fe_3O_4. *Philos. Mag.* **1970**, *22*, 163–174. [CrossRef]
29. Bednorz, J.G.; Müller, K.A. Possible high T_c superconductivity in the Ba−La−Cu−O system. *Z. Für Phys. B Condens. Matter* **1986**, *64*, 189–193. [CrossRef]
30. Cooper, J.; Alavi, B.; Zhou, L.; Beyermann, W.; Grüner, G. Thermoelectric power of some high-T_c oxides. *Phys. Rev. B* **1987**, *35*, 8794. [CrossRef]
31. Chen, J.; McEwan, C.; Wenger, L.; Logothetis, E. Determination of charge carriers in superconducting La-Ba-Cu-O by thermoelectric measurements. *Phys. Rev. B* **1987**, *35*, 7124. [CrossRef]
32. Mitra, N.; Trefny, J.; Yarar, B.; Pine, G.; Sheng, Z.; Hermann, A. Thermoelectric power of the Tl-Ca-Ba-Cu-O superconductor. *Phys. Rev. B* **1988**, *38*, 7064. [CrossRef]
33. Ohtaki, M.; Koga, H.; Tokunaga, T.; Eguchi, K.; Arai, H. Electrical transport properties and high-temperature thermoelectric performance of $(Ca_{0.9}M_{0.1})MnO_3$ (M = Y, La, Ce, Sm, In, Sn, Sb, Pb, Bi). *J. Solid State Chem.* **1995**, *120*, 105–111. [CrossRef]
34. Ohtaki, M.; Tsubota, T.; Eguchi, K.; Arai, H. High-temperature thermoelectric properties of $(Zn_{1-x}Al_x)O$. *J. Appl. Phys.* **1996**, *79*, 1816–1818. [CrossRef]
35. Terasaki, I.; Sasago, Y.; Uchinokura, K. Large thermoelectric power in $NaCo_2O_4$ single crystals. *Phys. Rev. B* **1997**, *56*, R12685–R12687. [CrossRef]
36. Masset, A.; Michel, C.; Maignan, A.; Hervieu, M.; Toulemonde, O.; Studer, F.; Raveau, B.; Hejtmanek, J. Misfit-layered cobaltite with an anisotropic giant magnetoresistance: $Ca_3Co_4O_9$. *Phys. Rev. B* **2000**, *62*, 166. [CrossRef]
37. Funahashi, R.; Matsubara, I.; Ikuta, H.; Takeuchi, T.; Mizutani, U.; Sodeoka, S. An oxide single crystal with high thermoelectric performance in air. *Jpn. J. Appl. Phys.* **2000**, *39*, L1127. [CrossRef]
38. Ishikawa, R.; Ono, Y.; Miyazaki, Y.; Kajitani, T. Low-Temperature Synthesis and Electric Properties of New Layered Cobaltite, Sr_xCoO_2. *Jpn. J. Appl. Phys.* **2002**, *41*, L337–L339. [CrossRef]
39. Kanno, T.; Yotsuhashi, S.; Adachi, H. Anisotropic thermoelectric properties in layered cobaltite A_xCoO_2 (A = Sr and Ca) thin films. *Appl. Phys. Lett.* **2004**, *85*, 739–741. [CrossRef]
40. Takashima, Y.; Zhang, Y.-Q.; Wei, J.; Feng, B.; Ikuhara, Y.; Cho, H.J.; Ohta, H. Layered cobalt oxide epitaxial films exhibiting thermoelectric ZT = 0.11 at room temperature. *J. Mater. Chem. A* **2021**, *9*, 274–280. [CrossRef]
41. Zhang, X.; Zhang, Y.; Wu, L.; Tsuruta, A.; Mikami, M.; Cho, H.J.; Ohta, H. $Ba_{1/3}CoO_2$: A Thermoelectric Oxide Showing a Reliable ZT of ~0.55 at 600 °C in Air. *ACS Appl. Mater. Interfaces* **2022**, *14*, 33355–33360. [CrossRef] [PubMed]
42. Okuda, T.; Nakanishi, K.; Miyasaka, S.; Tokura, Y. Large thermoelectric response of metallic perovskites: $Sr_{1-x}La_xTiO_3$ ($0 < \sim x < \sim 0.1$). *Phys. Rev. B* **2001**, *63*, 113104. [CrossRef]
43. Ohta, S.; Nomura, T.; Ohta, H.; Koumoto, K. High-temperature carrier transport and thermoelectric properties of heavily La-or Nb-doped $SrTiO_3$ single crystals. *J. Appl. Phys.* **2005**, *97*, 034106. [CrossRef]
44. Ohta, S.; Nomura, T.; Ohta, H.; Hirano, M.; Hosono, H.; Koumoto, K. Large thermoelectric performance of heavily Nb-doped $SrTiO_3$ epitaxial film at high temperature. *Appl. Phys. Lett.* **2005**, *87*, 092108. [CrossRef]
45. Lu, Z.L.; Zhang, H.R.; Lei, W.; Sinclair, D.C.; Reaney, I.M. High-Figure-of-Merit Thermoelectric La-Doped A-Site-Deficient $SrTiO_3$ Ceramics. *Chem Mater* **2016**, *28*, 925–935. [CrossRef]
46. Wang, J.; Zhang, B.-Y.; Kang, H.-J.; Li, Y.; Yaer, X.; Li, J.-F.; Tan, Q.; Zhang, S.; Fan, G.-H.; Liu, C.-Y.; et al. Record high thermoelectric performance in bulk $SrTiO_3$ via nano-scale modulation doping. *Nano Energy* **2017**, *35*, 387–395. [CrossRef]
47. Jang, J.S.; Kim, J.; Ghorpade, U.; Shin, H.H.; Gang, M.G.; Park, S.D.; Kim, H.-J.; Lee, D.S.; Kim, J.H. Comparison study of ZnO-based quaternary TCO materials for photovoltaic application. *J. Alloys Compd.* **2019**, *793*, 499–504. [CrossRef]
48. Kang, Y.; Yu, F.; Zhang, L.; Wang, W.; Chen, L.; Li, Y. Review of ZnO-based nanomaterials in gas sensors. *Solid State Ion.* **2021**, *360*, 115544. [CrossRef]
49. Le, A.T.; Ahmadipour, M.; Pung, S.-Y. A review on ZnO-based piezoelectric nanogenerators: Synthesis, characterization techniques, performance enhancement and applications. *J. Alloys Compd.* **2020**, *844*, 156172. [CrossRef]
50. Tsubota, T.; Ohtaki, M.; Eguchi, K.; Arai, H. Thermoelectric properties of Al-doped ZnO as a promising oxide material for high-temperature thermoelectric conversion. *J. Mater. Chem.* **1997**, *7*, 85–90. [CrossRef]
51. Wu, X.; Lee, J.; Varshney, V.; Wohlwend, J.L.; Roy, A.K.; Luo, T. Thermal Conductivity of Wurtzite Zinc-Oxide from First-Principles Lattice Dynamics—A Comparative Study with Gallium Nitride. *Sci. Rep.* **2016**, *6*, 22504. [CrossRef]
52. Wu, M.; Sun, D.; Tan, C.; Tian, X.; Huang, Y. Al-Doped ZnO Monolayer as a Promising Transparent Electrode Material: A First-Principles Study. *Materials* **2017**, *10*, 359. [CrossRef]
53. Jood, P.; Mehta, R.J.; Zhang, Y.; Peleckis, G.; Wang, X.; Siegel, R.W.; Borca-Tasciuc, T.; Dou, S.X.; Ramanath, G. Al-Doped Zinc Oxide Nanocomposites with Enhanced Thermoelectric Properties. *Nano Lett.* **2011**, *11*, 4337–4342. [CrossRef] [PubMed]
54. Park, K.; Seong, J.K.; Nahm, S. Improvement of thermoelectric properties with the addition of Sb to ZnO. *J. Alloys Compd.* **2008**, *455*, 331–335. [CrossRef]
55. Colder, H.; Guilmeau, E.; Harnois, C.; Marinel, S.; Retoux, R.; Savary, E. Preparation of Ni-doped ZnO ceramics for thermoelectric applications. *J. Eur. Ceram. Soc.* **2011**, *31*, 2957–2963. [CrossRef]

56. Liang, X. Thermoelectric Transport Properties of Fe-Enriched ZnO with High-Temperature Nanostructure Refinement. *ACS Appl. Mater. Interfaces* **2015**, *7*, 7927–7937. [CrossRef] [PubMed]
57. Ohtaki, M.; Araki, K.; Yamamoto, K. High Thermoelectric Performance of Dually Doped ZnO Ceramics. *J. Electron. Mater.* **2009**, *38*, 1234–1238. [CrossRef]
58. Acharya, S.; Yu, B.-K.; Hwang, J.; Kim, J.; Kim, W. High Thermoelectric Performance of ZnO by Coherent Phonon Scattering and Optimized Charge Transport. *Adv. Funct. Mater.* **2021**, *31*, 2105008. [CrossRef]
59. Biswas, S.; Singh, S.; Singh, S.; Chattopadhyay, S.; De Silva, K.K.H.; Yoshimura, M.; Mitra, J.; Kamble, V.B. Selective Enhancement in Phonon Scattering Leads to a High Thermoelectric Figure-of-Merit in Graphene Oxide-Encapsulated ZnO Nanocomposites. *ACS Appl. Mater. Interfaces* **2021**, *13*, 23771–23786. [CrossRef]
60. Zhou, Z.-F.; Ren, G.-K.; Tan, X.; Liu, R.; Liu, C.; Lin, Y.-H.; Nan, C.-W. Enhancing the thermoelectric performance of ZnO epitaxial films by Ga doping and thermal tuning. *J. Mater. Chem. A* **2018**, *6*, 24128–24135. [CrossRef]
61. Shimizu, S.; Bahramy, M.S.; Iizuka, T.; Ono, S.; Miwa, K.; Tokura, Y.; Iwasa, Y. Enhanced thermopower in ZnO two-dimensional electron gas. *Proc. Natl. Acad. Sci. USA* **2016**, *113*, 6438–6443. [CrossRef]
62. Hutson, A.R. Piezoelectric Scattering and Phonon Drag in ZnO and CdS. *J. Appl. Phys.* **1961**, *32*, 2287–2292. [CrossRef]
63. Bérardan, D.; Byl, C.; Dragoe, N. Influence of the Preparation Conditions on the Thermoelectric Properties of Al-Doped ZnO. *J. Am. Ceram. Soc.* **2010**, *93*, 2352–2358. [CrossRef]
64. Le, T.N.H.; Hou, F.; Vo, T.T.X.; Pham, Q.N.; Berardan, D.; Dragoe, N. Preparation and study of thermoelectric properties of fine grains $Gd_xZn_{1-x}O$. *Phys. Status Solidi A* **2013**, *210*, 2693–2698. [CrossRef]
65. Wang, Y.; Zhu, J.; Tang, W. Extracting the effective mass of electrons in transparent conductive oxide thin films using Seebeck coefficient. *Appl. Phys. Lett.* **2014**, *104*, 212103. [CrossRef]
66. Okhay, O.; Zlotnik, S.; Xie, W.; Orlinski, K.; Hortiguela Gallo, M.J.; Otero-Irurueta, G.; Fernandes, A.J.S.; Pawlak, D.A.; Weidenkaff, A.; Tkach, A. Thermoelectric performance of Nb-doped $SrTiO_3$ enhanced by reduced graphene oxide and Sr deficiency cooperation. *Carbon* **2019**, *143*, 215–222. [CrossRef]
67. Shi, X.-L.; Wu, H.; Liu, Q.; Zhou, W.; Lu, S.; Shao, Z.; Dargusch, M.; Chen, Z.-G. $SrTiO_3$-based thermoelectrics: Progress and challenges. *Nano Energy* **2020**, *78*, 105195. [CrossRef]
68. Acharya, M.; Jana, S.S.; Ranjan, M.; Maiti, T. High performance (ZT > 1) n-type oxide thermoelectric composites from earth abundant materials. *Nano Energy* **2021**, *84*, 105905. [CrossRef]
69. Zhang, Y.; Feng, B.; Hayashi, H.; Tohei, T.; Tanaka, I.; Ikuhara, Y.; Ohta, H. Thermoelectric phase diagram of the $SrTiO_3$–$SrNbO_3$ solid solution system. *J. Appl. Phys.* **2017**, *121*, 185102. [CrossRef]
70. Zhang, Y.; Sugo, K.; Cho, H.J.; Ohta, H. Thermoelectric phase diagram of the $SrTiO_3$-$LaTiO_3$ solid-solution system through a metal to Mott insulator transition. *J. Appl. Phys.* **2019**, *126*, 075104. [CrossRef]
71. Zhang, Y.; Cho, H.J.; Sugo, K.; Mikami, M.; Woo, S.; Jung, M.C.; Zhuang, Y.H.; Feng, B.; Sheu, Y.M.; Shin, W.; et al. Low thermal conductivity of $SrTiO_3-LaTiO_3$ and $SrTiO_3-SrNbO_3$ thermoelectric oxide solid solutions. *J. Am. Ceram. Soc.* **2021**, *104*, 4075–4085. [CrossRef]
72. Hicks, L.D.; Dresselhaus, M.S. Effect of quantum-well structures on the thermoelectric figure of merit. *Phys. Rev. B* **1993**, *47*, 12727–12731. [CrossRef]
73. Ohta, H.; Kim, S.; Mune, Y.; Mizoguchi, T.; Nomura, K.; Ohta, S.; Nomura, T.; Nakanishi, Y.; Ikuhara, Y.; Hirano, M.; et al. Giant thermoelectric Seebeck coefficient of a two-dimensional electron gas in $SrTiO_3$. *Nat. Mater.* **2007**, *6*, 129–134. [CrossRef]
74. Hung, N.T.; Hasdeo, E.H.; Nugraha, A.R.T.; Dresselhaus, M.S.; Saito, R. Quantum effects in the thermoelectric power factor of low-dimensional semiconductors. *Phys. Rev. Lett.* **2016**, *117*, 036602. [CrossRef] [PubMed]
75. Zhang, Y.; Feng, B.; Hayashi, H.; Chang, C.-P.; Sheu, Y.-M.; Tanaka, I.; Ikuhara, Y.; Ohta, H. Double thermoelectric power factor of a 2D electron system. *Nat. Commun.* **2018**, *9*, 2224. [CrossRef]
76. Banerjee, R.; Chatterjee, S.; Ranjan, M.; Bhattacharya, T.; Mukherjee, S.; Jana, S.S.; Dwivedi, A.; Maiti, T. High-Entropy Perovskites: An Emergent Class of Oxide Thermoelectrics with Ultralow Thermal Conductivity. *ACS Sustain. Chem. Eng.* **2020**, *8*, 17022–17032. [CrossRef]
77. Zheng, Y.; Zou, M.; Zhang, W.; Yi, D.; Lan, J.; Nan, C.-W.; Lin, Y.-H. Electrical and thermal transport behaviours of high-entropy perovskite thermoelectric oxides. *J. Adv. Ceram.* **2021**, *10*, 377–384. [CrossRef]
78. Koshibae, W.; Tsutsui, K.; Maekawa, S. Thermopower in cobalt oxides. *Phys. Rev. B* **2000**, *62*, 6869–6872. [CrossRef]
79. Tang, G.D.; Xu, F.; Zhang, D.W.; Wang, Z.H. Improving the spin entropy by suppressing Co^{4+} concentration in thermoelectric $Ca_3Co_4O_{9+\delta}$. *Ceram. Int.* **2013**, *39*, 1341–1344. [CrossRef]
80. Koshibae, W.; Maekawa, S. Effects of spin and orbital degeneracy on the thermopower of strongly correlated systems. *Phys. Rev. Lett.* **2001**, *87*, 236603. [CrossRef]
81. Wang, Y.; Rogado, N.S.; Cava, R.J.; Ong, N.P. Spin entropy as the likely source of enhanced thermopower in $Na_xCo_2O_4$. *Nature* **2003**, *423*, 425–428. [CrossRef]
82. Roca, A.G.; Mele, P.; Kijima-Aoki, H.; Fantechi, E.; Vejpravova, J.K.; Kalbac, M.; Kaneko, S.; Endo, T. *Surfaces and Interfaces of Metal Oxide Thin Films, Multilayers, Nanoparticles and Nano-composites: In Memory of Prof. Dr. Hanns-Ulrich Habermeier*; Springer: Berlin/Heidelberg, Germany, 2021.
83. Sales, B.C.; Jin, R.; Affholter, K.A.; Khalifah, P.; Veith, G.M.; Mandrus, D. Magnetic, thermodynamic, and transport characterization of $Na_{0.75}CoO_2$ single crystals. *Phys. Rev. B* **2004**, *70*, 174419. [CrossRef]

84. Cho, H.J.; Takashima, Y.; Nezu, Y.; Onozato, T.; Ohta, H. Anisotropic Heat Conduction in Ion-Substituted Layered Cobalt Oxides. *Adv. Mater. Interfaces* **2020**, *7*, 1901816. [CrossRef]
85. Huang, R.; Mizoguchi, T.; Sugiura, K.; Ohta, H.; Koumoto, K.; Hirayama, T.; Ikuhara, Y. Direct observations of Ca ordering in $Ca_{0.33}CoO_2$ thin films with different superstructures. *Appl. Phys. Lett.* **2008**, *93*, 181907. [CrossRef]

Disclaimer/Publisher's Note: The statements, opinions and data contained in all publications are solely those of the individual author(s) and contributor(s) and not of MDPI and/or the editor(s). MDPI and/or the editor(s) disclaim responsibility for any injury to people or property resulting from any ideas, methods, instructions or products referred to in the content.